ACS NANO
Cite This: ACS Nano XXXX, XXX, XXX–XXX
www.acsnano.org

ARTICLE

III–V Integration on Si(100): Vertical Nanospades

Lucas Güniat,[†] Sara Martí-Sánchez,[‡] Oscar Garcia,[¶] Mégane Boscardin,[†] David Vindice,[†] Nicolas Tappy,[†] Martin Friedl,[†] Wonjong Kim,[†] Mahdi Zamani,[†] Luca Francaviglia,[†] Akshay Balgarkashi,[†] Jean-Baptiste Leran,[†] Jordi Arbiol,[‡,§] and Anna Fontcuberta i Morral*[,∥,⊥]

[†]Laboratoire des Matériaux Semiconducteurs, École Polytechnique Fédérale de Lausanne, 1015 Lausanne, Switzerland
[‡]Catalan Institute of Nanoscience and Nanotechnology (ICN2), CSIC and BIST, Campus UAB, Bellaterra, 08193 Barcelona, Catalonia, Spain
[¶]UPC - Universitat Politècnica de Catalunya, Calle Jordi Girona, 1-3, 08034 Barcelona, Spain
[§]ICREA, Pg. Lluís Companys 23, 08010 Barcelona, Catalonia, Spain
[∥]Laboratory of Semiconductor Materials, Institute of Materials, École Polytechnique Fédérale de Lausanne, 1015 Lausanne, Switzerland
[⊥]Institute of Physics, École Polytechnique Fédérale de Lausanne, 1015 Lausanne, Switzerland

ABSTRACT: **III–V integration on Si(100) is a challenge: controlled vertical vapor liquid solid nanowire growth on this platform has not been reported so far. Here we demonstrate an atypical GaAs vertical nanostructure on Si(100), coined nanospade, obtained by a nonconventional droplet catalyst pinning. The Ga droplet is positioned at the tip of an ultrathin Si pillar with a radial oxide envelope. The pinning at the Si/oxide interface allows the engineering of the contact angle beyond the Young–Dupré equation and the growth of vertical nanospades. Nanospades exhibit a virtually defect-free bicrystalline nature. Our growth model explains how a pentagonal twinning event at the initial stages of growth provokes the formation of the nanospade. The optical properties of the nanospades are consistent with the high crystal purity, making these structures viable for use in integration of optoelectronics on the Si(100) platform.**

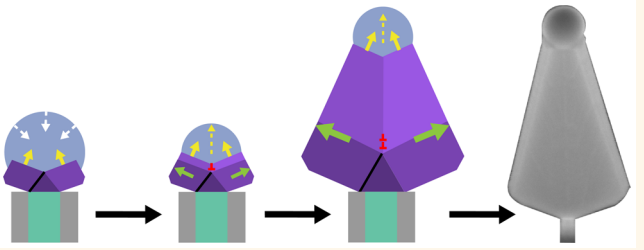

KEYWORDS: *nanospades, GaAs nanowires, nanowires, vertical growth, [100] growth, Si(100)*

Because of their exclusive and intriguing properties, semiconductor nanowires (NWs) have drawn increasing interest among researchers for their potential applications in a diverse range of fields, from p–n junction and high-performance transistors[1,2] to light-emitting diodes,[3] solar cells,[4−6] quantum computing,[7−9] terahertz detection,[10] and even biology.[11,12] To complete their path toward electronic and optoelectronic applications, their up-scalability and their compatibility with modern semiconductor processing need to be tackled. There is currently a joint effort in the NW community to bring the technology closer to compatibility with CMOS technology. A first step was replacing Au as the liquid catalyst in the vapor liquid solid (VLS) mechanism,[13] by other compounds, avoiding deep level traps in Si.[14−16] Highly uniform arrays have been successfully obtained by a self-catalyzed VLS method,[17−20] allowing Au-free opportunities for solar cells. Yet, those very promising results were exclusively obtained on Si wafers oriented in the [111] crystallographic direction, which is not the industry standard.

This work aims at implementing vertical, III–V-based self-catalyzed VLS-grown nanostructures on Si(100). Due to their preferential [111]B growth direction,[21] NWs spontaneously grow at an angle of 35° with the (100) surface, which would strongly compromise their functionality.[17] Several groups reported [100]-oriented III–V growth on III–V substrates using Au as a catalyst. This constitutes a limited number of systems, indicating the still open potential.[22−25] So far, controlled, defect-free [100]-oriented growth has not been demonstrated on the Si platform nor in a Au-free manner.

Here, we propose an original way of engineering the contact angle from the initial stages of growth by patterning Si(100) substrates into oxidized nanoscale pillars. This is one of the key elements that we propose to obtain Au-free vertically [100]-oriented flat nanostructures on the (100) Si platform, with a yield of currently 10% (number of structures over the total

Received: February 25, 2019
Accepted: April 30, 2019
Published: April 30, 2019

DOI: 10.1021/acsnano.9b01546
ACS Nano XXXX, XXX, XXX–XXX

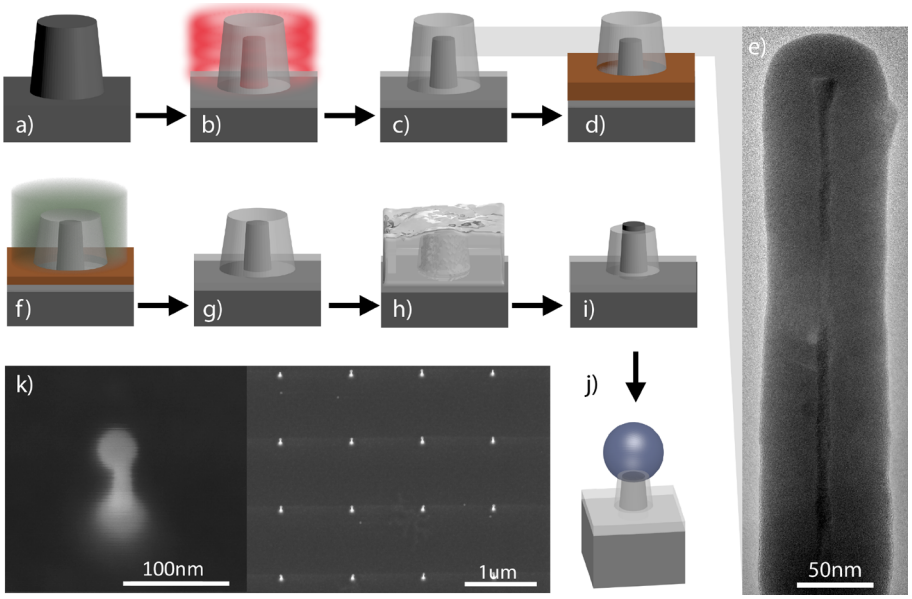

Figure 1. Scheme for the fabrication of the SiO_2 mask around (a) Si nanopillars. (b) A thermal oxidation is done at 900 °C (c) for nominal planar thicknesses ranging from 10 to 100 nm, as seen in the TEM micrograph (e). (d) A spin-coating of a polymeric protective layer and (f) a reactive ion etching offer a directional etching of the dielectric mask. (g) 5 nm is kept at the top of the pillar to keep the Si surface intact. A final hydrofluoric acid bath (h) permits uncovering the Si nanopillar's top. The sample is then introduced in the MBE chamber, and the growth is initiated with a liquid catalyst droplet predeposition (j). (k) SEM pictures of a Ga predeposition of 10 min on Si at 640 °C. The first picture depicts one pillar among the array shown in the second picture.

number of nucleation sites). These flat NW structures, called nanospades, exhibit high-quality crystalline structure with extremely few defects, rendering them suitable for photonic and energy-harvesting applications.

Several studies suggest that the configuration of the droplet catalyst determines the crystal phase,[18,21] growth direction,[23] polarity,[26,27] and uniformity.[28] Here, we engineer the liquid catalyst droplet in terms of size and contact angle before the VLS growth initiation itself to enable growth in the [100] direction. In doing so, a positive height-difference Si surface is crafted in the shape of a nanoscale pillar. Ga is then constrained at the tip using a SiO_2 mask. By varying the Ga predeposition time we make the droplet swell. This allows us to obtain contact angles that are higher than those expected for Ga on Si at equilibrium, the latter reported to be unstable for a reproducible NW growth.[28]

The Si nanopillar arrays are produced using a process similar to that of Varricchio *et al.*[29] First, a dotted pattern is defined on a 4 in. Si wafer using electron beam lithography. Then the pillars are defined by RIE (reactive ion etching) using a mixture of SF_6 and C_4F_8, followed by a buffered hydrofluoric acid bath for resist stripping. The bare Si nanopillar heights vary between 150 nm and 1 μm, and their diameters from 300 to 30 nm. In this study we keep the pitch distance at 1 μm. The pillars are subsequently oxidized at 900 °C, the oxide providing the role of selective growth mask, as depicted in Figure 1. The tips of the pillars are uncovered by a second RIE using a mixture of SF_6 and CHF_3. Finally, a diluted HF bath is used for an isotropic etching, ensuring the uncovering of the silicon pillar tip; see Figure 1.

Given the geometry of the Si pillar, its oxidation should reach a self-terminating regime, resulting in a sub-10 nm diameter.[30] This is due to the build-in of internal stresses upon oxidation, limiting the reaction rate at the interface. The strain tends to be compressive due to the incorporation of oxygen in the Si lattice.[31−33] The thermal mismatch between both species is also expected to produce further internal stresses (tensile) during the cooling.[34] Walavalkar *et al.*[30] showed by finite element simulations that the overall built-in stress in the Si is likely to be tensile at room temperature. The nature of the strain in our pillars is not central to this work, and it will be further clarified in follow-up studies.

Figure 1e shows a representative BF TEM (bright-field transmission electron microscopy) micrograph of an oxidized Si nanopillar. The nominal diameter of this pillar is 75 nm, and the oxidation time is set for a nominal thickness of 100 nm, at a temperature of 1000 °C. The contrast between SiO_2 and Si is the result of dynamical scattering at the interface and in the bulk Si, which is enhanced by the aforementioned stress.[30] The oxide is thicker at the sidewalls than at the top due to the increased surface exposed to oxygen during the thermal process, but also to the radial tensile strain in the bulk oxide, easing the early supply of oxidants radially.[31] The core Si pillar is 5 nm, indicating that the extent of the self-limiting oxide thickness can be reached in our system. The present work will focus on samples having a 15 nm Si core.

Several studies show that a deterministic contact angle engineering should serve in crystal phase engineering[21,35] and growth direction.[23] Therefore, we focused on the mastering of the wetting angle of the Ga droplets on top of the pillars. In order to vary the contact angle, we increased the total volume of the droplet by changing the Ga predeposition time. The resulting contact angles have been measured by cross-sectional SEM (scanning electron microscopy). Pillars from 35 to 270 nm in diameter have been fabricated, oxidized, and loaded in the MBE (molecular beam epitaxy) chamber, where a Ga equivalent flux of 0.15×10^{-6} Torr is kept for 10 min under an ultrahigh vacuum. The manipulator temperature is set at 740 °C, which corresponds to a substrate temperature of 650 °C. Figure 2a shows SEM images, representative of the

DOI: 10.1021/acsnano.9b01546
ACS Nano XXXX, XXX, XXX−XXX

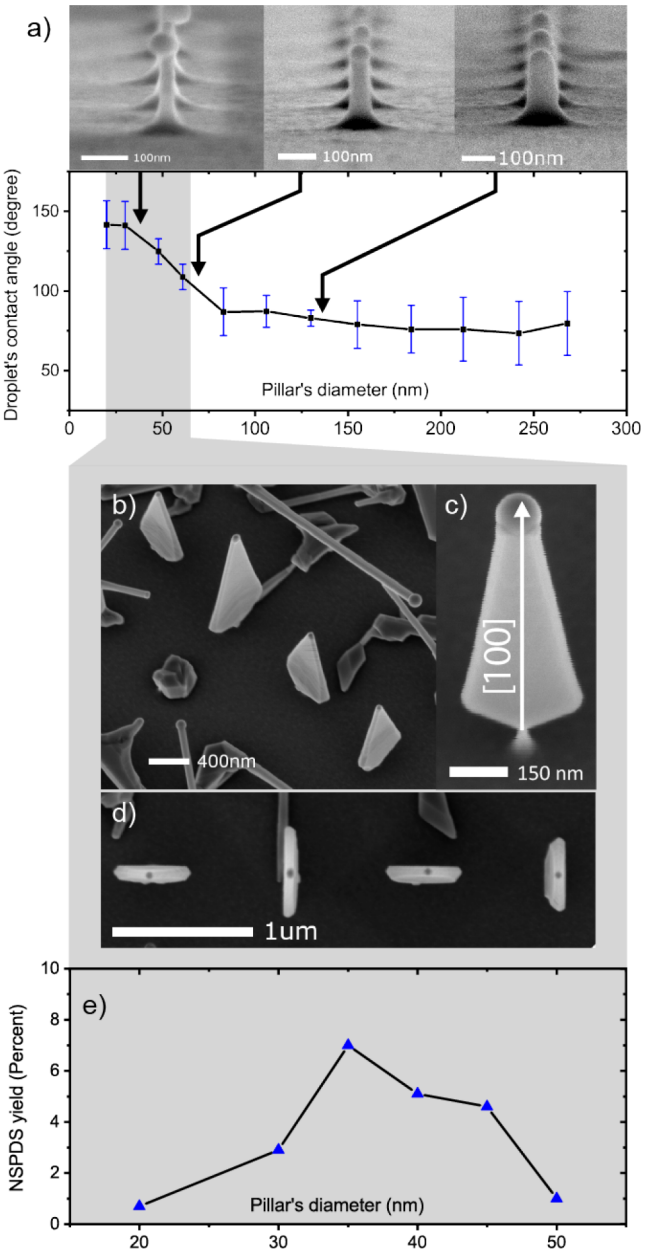

Figure 2. (a) Table showing the relation between Si pillars' diameter and the Ga droplets' contact angle, along with SEM images representing certain diameters. (b, c, and d) SEM pictures of GaAs nanospades on Si pillars and their growth range in the table. (e) Relation between the yield of nanospades (NSPDs) and pillar diameter for a 20 nm (nominal) oxide mask.

configurations obtained. We depict also the values of the contact angle as a function of the pillar diameter. We observe angles between 140° and 75°, from smaller to larger diameter pillars. There is a range between 40 and 100 nm where the contact angle varies almost linearly. For smaller pillars, the droplets fall down the side, which is expected to be detrimental for further MBE growth. For higher diameter pillars, the contact angle reaches the equilibrium value of liquid Ga on Si.[36] This variation of contact angle should translate to higher pillar diameters for longer deposition times, which shows the versatility and potential of this platform. It would be possible to tune the diameter and contact angle that one needs by correctly adapting the process parameters and growth conditions.

Figure2b to d highlight structures obtained in the range of contact angles marked in gray. They are oriented along the [100] direction. They exhibit a spade-like shape, substantiating their name. They can reach a high aspect ratio in two orthogonal directions. SEM pictures show the presence of a Ga droplet at the top, which confirms that they grow by the self-catalyzed VLS mechanism. However, their shape evolution throughout the growth appears to be a mixed contribution between VLS[19] and VS (vapor−solid),[37] the former for the vertical elongation and the later for the horizontal elongation. The nanospades (NSPDs) presented here have been grown using a Ga predeposition step of 10 min as mentioned in Figure2a, a Ga equivalent flux of 0.14×10^{-6} Torr, and a V/III ratio of 12. Figure 2e indicates the yield as a function of the pillar diameter. We can reach a maximum yield close to 10% for 35 nm diameter pillars. The other pillars contain [111]B-oriented GaAs NWs and parasitic growth. The yield drastically decreases for pillars larger than 50 nm, plummeting to a value of 1%. The low yield in smaller pillars can be explained by the Ga droplet falling down the side and, in larger pillars, by the energy of formation of the initial seed, as explained further below.

NSPDs have been transferred flat on a TEM grid and observed using an Cs-corrected TEM. Figure 3 shows a high-angle annular dark-field scanning transmission electron microscopy (HAADF-STEM) general overview of the studied nanospade in (a), details obtained on the tip in (b) and (c), and a color map showing the structure at the base in (d). Polarities have been resolved by an intensity analysis, as heavier atoms (As) appear brighter. The overall structure exhibits an original crystalline structure. The base is composed of several symmetrical twins and polarities, while the body consists of a bicrystal. Figure 3d shows the presence of a [100]-oriented domain (light blue) that is A-polar, Ga terminated, which is believed to be in epitaxial relation with the Si. This [100]A-oriented domain creates a truncated octahedron with (111)A facets where twin boundaries form upon further growth, showing a multiple-order twinning mechanism.[38] A similar mechanism has been observed in [111]-B-oriented nanowire growth. It consists of the formation of successive twinning events in the three dimensions of space, resulting in well-defined modifications in the nanowire orientation with the substrate. Interestingly, after the first monolayer, one side exhibits a change of polarity (dark blue) with respect to the other side (red). To the best of our knowledge, this is one of the first reports of a polarity change during nanostructure growth. Due to its high energetic cost, this polarity change should be very unlikely to happen.[39] Its function is the conservation of the overall polarity in both sides of the truncated octahedral seed. This structure is similar to the InAs V-shaped membranes obtained by Conesa-Boj *et al.*,[40] where an [100]-oriented truncated octahedron is the seed of two [111]B-oriented "wings".

In the case of NSPDs, the top of the seed exhibits the formation of two extra twins forming an angle of 70.53° with the vertical direction, giving rise to a pentagonal grain boundary structure. It is important to note that a regular pentagon would have angles of exactly 72°, while the {111} twinning happens at 70.53°. There is a 7.32° mismatch that is relaxed by the creation of dislocations in the first few nanometers of the vertical twin boundary. This fact is clearly

DOI: 10.1021/acsnano.9b01546
ACS Nano XXXX, XXX, XXX−XXX

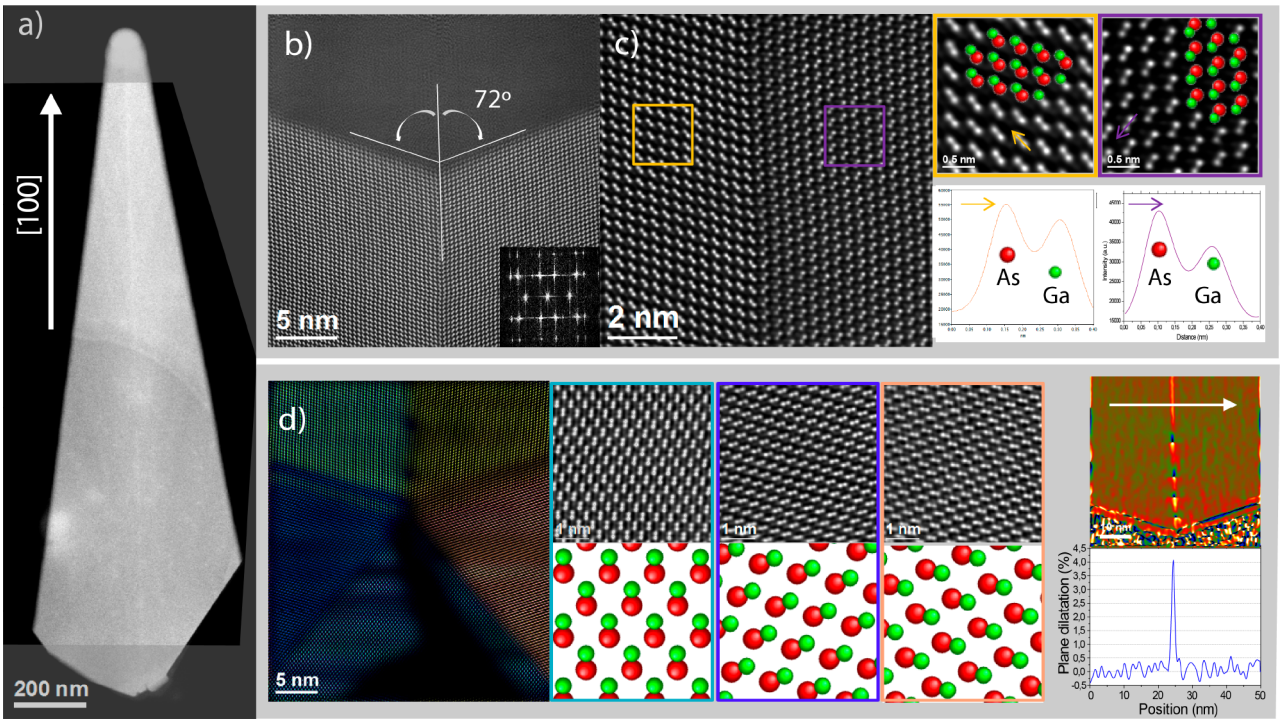

Figure 3. HAADF STEM study of the GaAs NSPD shown in (a). (b) Growth front. (c) Central vertical twin with the polarity of each side. (d) Color structural map of the penta-twin at the base of the NSPD and the resolved polarities of each grain. A geometrical phase analysis study at the base shows the plane dilatation on the vertical twin (the strain is around 4%), along with dislocations on this boundary. Far away from the base, after a partial relaxation, the remanent strain in the boundary along the [100] direction is shown to be 2.5%.

visible in Figure 3d, where a GPA (geometrical phase analysis) study shows four misfit dislocations aligned on this domain boundary, and a plane dilatation of 4% is measured in the upper region. Figure 3c demonstrates that the structure succeeds in compensating for this mismatch, forming a virtually defect-free bicrystal.

Twinning with 5-fold symmetry has been observed in a variety of systems such as copper bulk[41] and NWs,[42] diamond,[43] Au,[44,45] but also GaAs in a study by Däweritz *et al.*,[46] where RHEED (reflection high-energy electron diffraction) examinations of defects on GaAs(001) reveal a structure analogous to the nanospade pentagonal seed. L. D. Marks[47] presents modified Wulff constructions for twinned nanoparticles, including 5-fold symmetry twins. He divides the twinned particles into different segments bounded by the twin planes. Each segment possesses planes with given surface energies γ_x. For each twin boundary, the energy is divided into two fractions, $\alpha\gamma$ and $(1 - \alpha)\gamma$, respectively, for the segments sharing this twin, where α is defined as the partition coefficient. The lowest energy crystal shape is then determined by Wulff construction for each of the defined segments, with the twin boundaries included as pseudosurface facets. The volume partition and geometric constraints are also taken into considerations. If values of α_x can be found where the segments still assemble to a complete particle, a local energy minimum may be found. The symmetrical case of $\alpha = \frac{1}{2}$ and equal volumes for each segment is always a solution and proven to be a true minimum. In the case of a 5-fold symmetry twinned particle, a second solution arises by placing two asymmetric twin relationships, pushing the meeting point of the five segments well away from the particle center. This case resonates with the NSPDs, where the pentagonal twin is located very close to the (100) substrate surface, *i.e.*, at the base of the structure. Despite the fact that our system is mainly kinetically driven, it is worth noting that such asymmetry can be caused by a difference in the twinning energies due to the polarity inversion.

Interestingly, Figure 3b shows the growth front formed by two {111} planes that seem to grow simultaneously. This is known as the twin plane re-entrant (TPRE) mechanism, observed recently in the growth of GaAs NWs,[48] but also in other material systems such as ZnSe,[49] InSb,[50] and Si or Ge,[51,52] but also in the bulk. Bulk TPRE configuration permits a fast expansion of platelets creating re-entrant edges, which at the same time serve as active nucleation sites. As elucidated by R. S. Wagner,[53] the TPRE mechanism in the bulk needs at least two twinning events to be stable. Otherwise, a single twin would rapidly outgrow itself. The platelet growth rate would then be limited by the nucleation at the ridge, which is significantly smaller. Nonetheless, Gamalski *et al.*[52] showed that the nanoscale geometry allows steady-state growth based on a single twin boundary. Here, the growth rate of the structure is completely determined by the nucleation rate at the twin rather than at the triple-phase line. This prevents any of the sides of the twin from outgrowing the other. Thus, the structure remains symmetrical despite having one B-polar and one A-polar orientation, which are known to have different nucleation and growth rates.[26,54−56]

One should note that contact angle engineering resulted into a maximized yield of 8%, which is relatively low. We believe this is related to the growth mechanism, combining both a polarity inversion and a 5-fold symmetry twinning. Nonetheless, we think that the yield could be further controlled. In particular, we believe the engineering of the pillar surface by nanofaceting could enable the TPRE mechanism without the

DOI: 10.1021/acsnano.9b01546
ACS Nano XXXX, XXX, XXX−XXX

need of the pentagonal twin structure. In addition, introduction of impurities or change in the growth regime may as well increase the probability of 5-fold symmetry twinning and TPRE.[57,58]

We now proceed with the proposal of a growth model for the NSPDs, combining our observations with other groups' results on the formation of penta-twins[59] and the *in situ* TEM observation of NW growth.[52,54,60] Figure 4 depicts the model we propose. The process starts with the pinning of the Ga droplet at the Si/oxide interface at the pillar tip. After a brief incubation time, the nucleation of GaAs layers starts. Initially, a [100] Ga-oriented pyramid forms (truncated octahedron), with the two opposite (111)A and (111)B facets. Overall, this results in five liquid/solid growth fronts, leading to a decrease in the size of the droplet due to Ga consumption. The [111]-oriented lateral fronts outgrow the (100) plane, reaching the triple phase boundary, ceasing to be expanded by the VLS mechanism. After the termination of the [100]-oriented domain, a double-twinning event occurs, modifying the orientation of the growth front. As a consequence, the bicrystals constituting GaAs NSPD's main core are formed and grow perpendicularly to the substrate. The growth will proceed by the TPRE/VLS mechanism at the top, pushing the structure up. Additional VS growth expands the structure laterally, in two [110] directions (as is the case for typical NW growth).

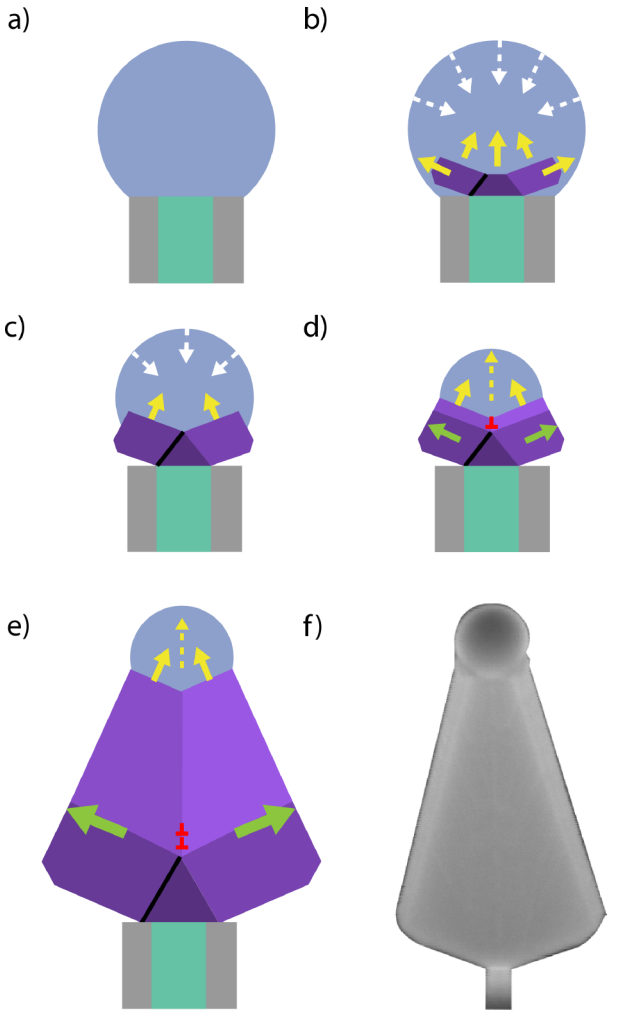

Figure 4. Schematic growth model depicting in (a) the Ga droplet pinning, (b) followed by the start of the growth with three VLS growth fronts: a [100]-oriented and two [111]-oriented. The droplet shrinks progressively, leading to a transient mode (c) that is followed by (d) the penta-twin formation. The growth is further continued by the VLS/twin plane re-entrant (TPRE) on top and the VS on the sides. The polarity inversion is highlighted by the dark line, the VLS growth by yellow arrows, and the VS growth by green arrows. Dislocations formed by the built-in strain are represented by inverted "T"-shapes. (f) Tilted SEM view of a generic nanospade.

The presence of twins and dislocations in semiconductor architectures could potentially reduce their viability for further applications. In order to assess the impact of the crystalline structure on the optoelectronic properties, we characterized them by luminescence. In particular, we were interested in obtaining signal of the defects at the NSPD base. For this, we increased the volume of the NSPDs by vapor−solid growth akin to ref 61. The thick NSPDs are then transferred flat onto a Au-coated Si substrate. Figure 5 shows in (a) the micro-photoluminescence (μPL) spectra at 300 and 8 K and in (b) the cathodoluminescence (CL) spectra line scan.

In the RT (room temperature) μPL spectra, an emission at 867 nm, which corresponds to the band gap of GaAs, can be seen, along with a secondary much weaker peak slightly above noise level between 900 and 930 nm. This secondary feature becomes almost invisible at 8 K, where the overall signal—corresponding to the free-exciton recombination emission in bulk GaAs at 1.51 eV and to an impurity-related band between 1.48 and 1.5 eV[62−64]—is much higher. We attribute this weaker peak to defects at the base of the nanostructure. These defects exhibit energy levels with a limited density of states, as is usually the case for localized defects. As expected, emission from such states saturates with increasing excitation power, especially at low temperature, where recombination lifetimes are longer. By looking at the CL spectra in (b), the same feature is observed. The line scan along the NSPD unveils its origin at the base, close to the semioctahedron seed, the polarity inversion, and dislocations. It is concluded that those radiative transitions occur at the mentioned defects and are not observed in the rest of the structure. The CL spectra also show a decrease of the 819 nm exciton emission in the upper half of the structure. This is explained by the increase of the surface to volume ratio, quenching the emission by nonradiative recombinations at the GaAs surface. Further CL characterizations using AlGaAs shells and GaAs quantum wells are envisioned, along with a study on self-assembled quantum dots[65,66] for assessing the impact of the NSPD structure on their formation.

CONCLUSION

To conclude, we have successfully designed and built an innovative Si platform for self-catalyzed VLS growth, consisting of etched nanopillars covered by a thermal oxide. The presence of a self-limiting oxidation effect permits a Si exposure in the chamber that is under 10 nm, enabling nonequilibrium growth conditions. The appearance of [100]-vertically oriented nanostructures, called nanospades, is a proof of the viability of this approach. A yield of NSPDs up to 10% has been obtained. This is expected to increase with further growth optimization. Overall, the NSPDs are mainly a bicrystal nucleated by penta-twins at the base. The optical properties are clearly consistent with high-quality GaAs. The penta-twin exhibits weak luminescence below the GaAs band gap, spatially

DOI: 10.1021/acsnano.9b01546
ACS Nano XXXX, XXX, XXX−XXX

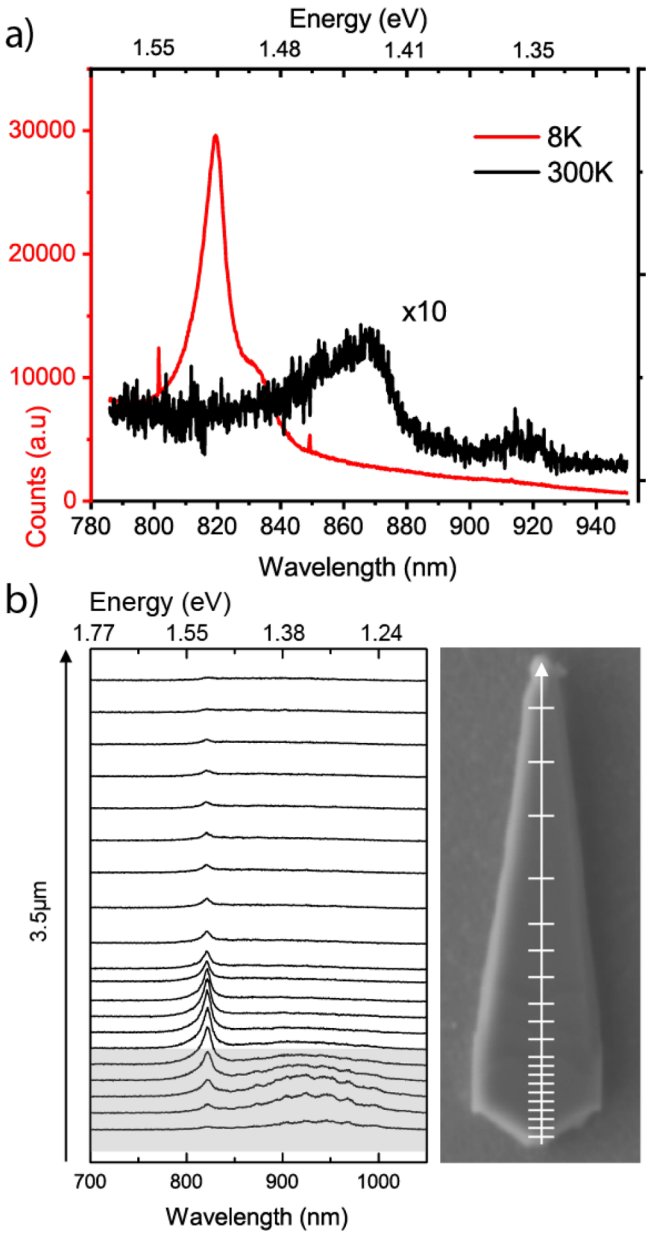

Figure 5. (a) Photoluminescence and (b) 10 K cathodoluminescence characterization of two different NSPDs. The vertical lines in the SEM picture show where the CL spectra have been acquired. Both studies show the presence of low-energy peaks linked spatially with the penta-twin and polarity inversion region.

localized at the base of the nanostructure. The NSPDs are promising structures for room-temperature lasing, energy harvesting, and photonic applications.[61,67−71]

METHODS/EXPERIMENTAL

A 2 min 600 W O_2 plasma power in a TEPLA GigaBatch is done on a 100 mm Si wafer for surface activation before exposing it to e-beam lithography with a Vistec EBPG5000ES and using Dow Corning HSQ 006 (hydrogen silsesquioxane) as a resist. The dose used is 2740 $\mu C/cm^2$ for all the pillars' diameters. The wafer is then developed using a commercial solution of Microposit^R MF^R CD26 for 2 min and rinsed sequentially with water, acetone, and propan-2-ol. A 2 min 600 W O_2 plasma power in a TEPLA GigaBatch is done for further cross-linking the HSQ. The wafer is then introduced in an Alcatel AMS200 DSE reactive ion etcher, where a customized recipe using SF_6 and C_4F_8 is used for creating the pillars. A buffered hydrofluoric acid (7:1) bath is then used for 2 min to remove any trace of resist. A thermal oxidation is then done at 900 °C for a variable amount of time depending on the desired oxide thickness. After the oxide growth, a 20 nm styrene methyl acrylate based resist (ZEP) film is spin coated and heated for 2 min at 180 °C for polymerization. The sample is inserted in an Oxford Plasmalab system 80 PLUS using a mixture of SF_6 and CHF_3 at 100 W plasma power for 40 s to uncover the pillars. Ten minutes of O_2 plasma permits the removal of the resist, and a last cleaning involving a 5 min acetone bath, a 2 min propan-2-ol bath, and a 35 s HF bath at 1% concentration makes the sample ready for growth.

The growths are conducted in a DCA MBE chamber under a Ga BEP (beam equivalent pressure) of 0.14×10^{-6} Torr and an As BEP of 1.7×10^{-6} Torr for 45 min. The samples were characterized by SEM using a Zeiss Merlin and by HAADF STEM using a probe-corrected FEI Titan 60-300 equipped with a high-brightness field emission gun (XFEG) and a CETCOR corrector from CEOS. The μPL measurements were done using an in-house built setup using a 532 nm sapphire optically pumped semiconductor laser, and the CL using an Attolight Rosa 4634 SEM-CL microscope at 5 keV.

AUTHOR INFORMATION

Corresponding Author

*E-mail: anna.fontcuberta-morral@epfl.ch.

ORCID

Lucas Güniat: 0000-0001-7883-4433
Jordi Arbiol: 0000-0002-0695-1726
Anna Fontcuberta i Morral: 0000-0002-5070-2196

Notes

The authors declare no competing financial interest.

ACKNOWLEDGMENTS

L.G. thanks the MBE team for the very nice coordination and collaboration. We thank also the SNF and QSIT for funding the projects 200021_169908 and IZLRZ2_163861. S.M.S. acknowledges funding from "Programa Internacional de Becas "la Caixa"-Severo Ochoa". J.A. and S.M.S. acknowledge funding from Generalitat de Catalunya 2017 SGR 327 and the Spanish MINECO project ENE2017-85087-C3. ICN2 is supported by the Severo Ochoa program from Spanish MINECO (Grant No. SEV-2017-0706) and is funded by the CERCA Programme/Generalitat de Catalunya. Part of the present work has been performed in the framework of Universitat Autònoma de Barcelona Materials Science Ph.D. program. The HAADF-STEM microscopy was conducted in the Laboratorio de Microscopias Avanzadas at Instituto de Nanociencia de Aragon-Universidad de Zaragoza. The authors acknowledge the LMA-INA for offering access to their instruments and expertise.

REFERENCES

(1) Cui, Y.; Wei, Q.; Park, P.; Lieber, C. M.; Park, H. Nanowire Nanosensors for Highly Sensitive and Selective Detection of Biological and Chemical Species. *Science (Washington, DC, U. S.)* **2001**, *293*, 1289−1292.

(2) Chuang, S.; Gao, Q.; Kapadia, R.; Ford, A. C.; Guo, J.; Javey, A. Ballistic InAs Nanowire Transistors. *Nano Lett.* **2013**, *13*, 555−558.

(3) Könenkamp, R.; Word, R. C.; Schlegel, C. Vertical Nanowire Light-emitting Diode. *Appl. Phys. Lett.* **2004**, *85*, 6004−6006.

(4) Suh, D. I.; Lee, S. Y.; Kim, T. H.; Chun, J. M.; Suh, E. K.; Yang, O. B.; Lee, S. K. The Fabrication And Characterization Of Dye-sensitized Solar Cells With A Branched Structure Of ZnO Nanowires. *Chem. Phys. Lett.* **2007**, *442*, 348−353.

(5) Krogstrup, P.; Jørgensen, H. I.; Heiss, M.; Demichel, O.; Holm, J. V.; Aagesen, M.; Nygard, J.; Fontcuberta i Morral, A. Single-

DOI: 10.1021/acsnano.9b01546
ACS Nano XXXX, XXX, XXX−XXX

nanowire Solar Cells Beyond The Shockley−queisser Limit. *Nat. Photonics* **2013**, *7*, 306−310.
(6) Wallentin, J.; Anttu, N.; Asoli, D.; Huffman, M.; Aberg, I.; Magnusson, M. H.; Siefer, G.; Fuss-Kailuweit, P.; Dimroth, F.; Witzigmann, B.; Xu, H. Q.; Samuelson, L.; Deppert, K.; Borgström, M. T. InP Nanowire Array Solar Cells Achieving 13.8% Efficiency By Exceeding The Ray Optics Limit. *Science* **2013**, *339*, 1057−1060.
(7) Mourik, V.; Zuo, K.; Frolov, S. M.; Plissard, S. R.; Bakkers, E. P. A. M.; Kouwenhoven, L. P. Signatures of Majorana Fermions in Hybrid Superconductor-Semiconductor Nanowire Devices. *Science (Washington, DC, U. S.)* **2012**, *336*, 1003−1007.
(8) Liu, Z.-h.; Li, R. Spin-relaxation Anisotropy In A Nanowire Quantum Dot With Strong Spin-orbit Coupling. *AIP Adv.* **2018**, *8*, 0751151.
(9) Manolescu, A.; Sitek, A.; Osca, J.; Serra, L.; Gudmundsson, V.; Stanescu, T. D. Majorana States In Prismatic Core-shell Nanowires. *Phys. Rev. B: Condens. Matter Mater. Phys.* **2017**, *96*, 13 DOI: 10.1103/PhysRevB.96.125435.
(10) Peng, K.; Parkinson, P.; Gao, Q.; Boland, J. L.; Li, Z.; Wang, F.; Mokkapati, S.; Fu, L.; Johnston, M. B.; Tan, H. H.; Jagadish, C. Single n+-i-n+ InP Nanowires For Highly Sensitive Terahertz Detection. *Nanotechnology* **2017**, *28*, 125202−9.
(11) Mattsson, K.; Adolfsson, K.; Ekvall, M. T.; Borgström, M. T.; Linse, S.; Hansson, L. A.; Cedervall, T.; Prinz, C. N. Translocation Of 40 Nm Diameter Nanowires Through The Intestinal Epithelium Of Daphnia Magna. *Nanotoxicology* **2016**, *10*, 1160−1167.
(12) Gautam, V.; Naureen, S.; Shahid, N.; Gao, Q.; Wang, Y.; Nisbet, D.; Jagadish, C.; Daria, V. R. Engineering Highly Interconnected Neuronal Networks On Nanowire Scaffolds. *Nano Lett.* **2017**, *17*, 3369−3375.
(13) Wagner, R. S.; Ellis, W. C. Vapor-Liquid-Sold Mechanism of Single Crystal Growth. *Appl. Phys. Lett.* **1964**, *4*, 89−90.
(14) Colombo, C.; Spirkoska, D.; Frimmer, M.; Abstreiter, G.; Fontcuberta I Morral, A. Ga-assisted Catalyst-free Growth Mechanism Of GaAs Nanowires By Molecular Beam Epitaxy. *Phys. Rev. B: Condens. Matter Mater. Phys.* **2008**, *77*, 155326−5.
(15) Fontcuberta I Morral, A.; Colombo, C.; Abstreiter, G.; Arbiol, J.; Morante, J. R. Nucleation Mechanism Of Gallium-assisted Molecular Beam Epitaxy Growth Of Gallium Arsenide Nanowires. *Appl. Phys. Lett.* **2008**, *92*, 10−13.
(16) Ho, J. C.; Razavi, H.; Ford, A. C.; Altoe, V.; Aloni, S.; Ergen, O.; Fan, Z.; Javey, A. Synthesis, Contact Printing, And Device Characterization Of Ni-catalyzed, Crystalline InAs Nanowires. *Nano Res.* **2008**, *1*, 32−39.
(17) Russo-Averchi, E.; Vukajlovic Plestina, J.; Tütüncüoglu, G.; Matteini, F.; Dalmau-Mallorquí, A.; De La Mata, M.; Rüffer, D.; Potts, H. A.; Arbiol, J.; Conesa-Boj, S.; Fontcuberta I. Morral, A. High Yield Of GaAs Nanowire Arrays On Si Mediated By The Pinning And Contact Angle Of Ga. *Nano Lett.* **2015**, *15*, 2869−2874.
(18) Kim, W.; Dubrovskii, V. G.; Vukajlovic-Plestina, J.; Tütüncüoglu, G.; Francaviglia, L.; Güniat, L.; Potts, H.; Friedl, M.; Leran, J. B.; Fontcuberta I Morral, A. Bistability of Contact Angle and Its Role in Achieving Quantum-Thin Self-Assisted GaAs nanowires. *Nano Lett.* **2018**, *18*, 49−57.
(19) Plissard, S.; Larrieu, G.; Wallart, X.; Caroff, P. High Yield Of Self-catalyzed GaAs Nanowire Arrays Grown On Silicon Via Gallium Droplet Positioning. *Nanotechnology* **2011**, *22*, 275602−7.
(20) Munshi, A. M.; Dheeraj, D. L.; Fauske, V. T.; Kim, D. C.; Huh, J.; Reinertsen, J. F.; Ahtapodov, L.; Lee, K. D.; Heidari, B.; Van Helvoort, A. T.; Fimland, B. O.; Weman, H. Position-controlled Uniform GaAs Nanowires On Silicon Using Nanoimprint Lithography. *Nano Lett.* **2014**, *14*, 960−966.
(21) Glas, F.; Harmand, J. C.; Patriarche, G. Why Does Wurtzite Form In Nanowires Of III-V Zinc Blende Semiconductors? *Phys. Rev. Lett.* **2007**, *99*, 146101−4.
(22) Björk, M. T.; Ohlsson, B. J.; Sass, T.; Persson, A. I.; Thelander, C.; Magnusson, M. H.; Deppert, K.; Wallenberg, L. R.; Samuelson, L. One-dimensional Heterostructures In Semiconductor Nanowhiskers. *Appl. Phys. Lett.* **2002**, *80*, 1058−1060.
(23) Wang, J.; Plissard, S. R.; Verheijen, M. A.; Feiner, L. F.; Cavalli, A.; Bakkers, E. P. A. M. Reversible Switching Of InP Nanowire Growth Direction By Catalyst Engineering. *Nano Lett.* **2013**, *13*, 3802−3806.
(24) Mikkelsen, A.; Eriksson, J.; Lundgren, E.; Andersen, J. N.; Weissenrieder, J.; Seifert, W. The Influence Of Lysine On InP(001) Surface Ordering And Nanowire Growth. *Nanotechnology* **2005**, *16*, 2354−2359.
(25) Wang, J.; Plissard, S.; Hocevar, M.; Vu, T. T.; Zehender, T.; Immink, G. G.; Verheijen, M. A.; Haverkort, J.; Bakkers, E. P. Position-controlled [100] InP Nanowire Arrays. *Appl. Phys. Lett.* **2012**, *100*, 053107−4.
(26) Yuan, X.; Caroff, P.; Wong-Leung, J.; Fu, L.; Tan, H. H.; Jagadish, C. Tunable Polarity in a III-V Nanowire by Droplet Wetting and Surface Energy Engineering. *Adv. Mater.* **2015**, *27*, 6096−6103.
(27) Zamani, R. R.; Gorji Ghalamestani, S.; Niu, J.; Sköld, N.; Dick, K. A. Polarity And Growth Directions In Sn-seeded GaSb Nanowires. *Nanoscale* **2017**, *9*, 3159−3168.
(28) Matteini, F.; Tütüncüoglu, G.; Mikulik, D.; Vukajlovic-Plestina, J.; Potts, H.; Leran, J.-B.; Carter, W. C.; Fontcuberta i Morral, A. Impact Of The Ga Droplet Wetting, Morphology, And Pinholes On The Orientation Of GaAs Nanowires. *Cryst. Growth Des.* **2016**, *16*, 5781−5786.
(29) Varricchio, S. S. G.; Cyrille, H.; Arnaud, B.; Philippe, R. Fabrication Of Multilayered Nanofluidic Membranes Through Silicon Templates. *Nanoscale* **2015**, *7*, 20451−20459.
(30) Walavalkar, S. S.; Hofmann, C. E.; Homyk, A. P.; Henry, M. D.; Atwater, H. A.; Scherer, A. Tunable Visible And Near-IR Emission From Sub-10 Nm Etched Single-crystal Si Nanopillars. *Nano Lett.* **2010**, *10*, 4423−4428.
(31) Kao, D.-B.; McVittie, J.; Nix, W.; Saraswat, K. Two-dimensional Thermal Oxidation Of Silicon. II. Modeling Stress Effects In Wet Oxides. *IEEE Trans. Electron Devices* **1988**, *35*, 25−37.
(32) Liu, H. I.; Biegelsen, D. K.; Ponce, F. A.; Johnson, N. M.; Pease, R. F. W. Self-limiting Oxidation For Fabricating Sub-5 Nm Silicon Nanowires. *Appl. Phys. Lett.* **1994**, *64*, 1383−1385.
(33) Cui, H.; Wang, C. X.; Yang, G. W. Origin Of Self-limiting Oxidation Of Si Nanowires. *Nano Lett.* **2008**, *8*, 2731−2737.
(34) Skibitzki, O.; Prieto, I.; Kozak, R.; Capellini, G.; Zaumseil, P.; Arroyo Rojas Dasilva, Y.; Rossell, M. D.; Erni, R.; Von Kanel, H.; Schroeder, T. Structural and Optical Characterization Of GaAs Nanocrystals Selectively Grown On Si Nano-tips By MOVPE. *Nanotechnology* **2017**, *28*, 135301−10.
(35) Jacobsson, D.; Panciera, F.; Tersoff, J.; Reuter, M. C.; Lehmann, S.; Hofmann, S.; Dick, K. A.; Ross, F. M. Interface Dynamics And Crystal Phase Switching In GaAs Nanowires. *Nature* **2016**, *531*, 317−322.
(36) Matteini, F.; Tütüncüoglu, G.; Potts, H.; Jabeen, F.; Fontcuberta I Morral, A. Wetting of Ga on SiOx and Its Impact on GaAs Nanowire Growth. *Cryst. Growth Des.* **2015**, *15*, 3105−3109.
(37) Tutuncuoglu, G.; De La Mata, M.; Deiana, D.; Potts, H.; Matteini, F.; Arbiol, J.; Fontcuberta I Morral, A. Towards Defect-free 1-D GaAs/AlGaAs Heterostructures Based On GaAs Nanomembranes. *Nanoscale* **2015**, *7*, 19453−19460.
(38) Uccelli, E.; Arbiol, J.; Magen, C.; Krogstrup, P.; Russo-Averchi, E.; Heiss, M.; Mugny, G.; Morier-Genoud, F.; Nygard, J.; Morante, J. R.; Fontcuberta I Morral, A. Three-dimensional Multiple-order Twinning Of Self-catalyzed GaAs Nanowires On Si Substrates. *Nano Lett.* **2011**, *11*, 3827−3832.
(39) De La Mata, M.; Magen, C.; Gazquez, J.; Utama, M. I. B.; Heiss, M.; Lopatin, S.; Furtmayr, F.; Fernández-Rojas, C. J.; Peng, B.; Morante, J. R.; Rurali, R.; Eickhoff, M.; Fontcuberta I Morral, A.; Xiong, Q.; Arbiol, J. Polarity Assignment in ZnTe, GaAs, ZnO, and GaN-AlN Nanowires From Direct Dumbbell Analysis. *Nano Lett.* **2012**, *12*, 2579−2586.
(40) Conesa-Boj, S.; Russo-Averchi, E.; Dalmau-Mallorqui, A.; Trevino, J.; Pecora, E. F.; Forestiere, C.; Handin, A.; Ek, M.; Zweifel, L.; Wallenberg, L. R.; Rüffer, D.; Heiss, M.; Troadec, D.; Dal Negro, L.; Caroff, P.; Fontcuberta i Morral, A. Vertical III−V″ V-Shaped

DOI: 10.1021/acsnano.9b01546
ACS Nano XXXX, XXX, XXX−XXX

Nanomembranes Epitaxially Grown on a Patterned Si[001] Substrate and Their Enhanced Light Scattering. *ACS Nano* **2012**, *6*, 10982−10991.
(41) Huang, P.; Dai, G. Q.; Wang, F.; Xu, K. W.; Li, Y. H. Fivefold Annealing Twin In Nanocrystalline Cu. *Appl. Phys. Lett.* **2009**, *95*, 10−13.
(42) Kim, C.; Gu, W.; Briceno, M.; Robertson, I. M.; Choi, H.; Kim, K. Copper Nanowires With A Five-twinned Structure Grown By Chemical Vapor Deposition. *Adv. Mater.* **2008**, *20*, 1859−1863.
(43) Narayan, J.; Srivatsa, A. R.; Ravi, K. V. Mechanism Of Formation Of 110 Oriented Fivefold Microcrystallites In Diamond Films. *Appl. Phys. Lett.* **1989**, *54*, 1659−1661.
(44) Hofmeister, H.; Haefke, H.; Panov, A. Growth Of Gold Particles Vapour-deposited Onto Silver Bromide Films. *J. Cryst. Growth* **1982**, *58*, 500−506.
(45) Piella, J.; Merkoçi, F.; Genç, A.; Arbiol, J.; Bastús, N. G.; Puntes, V. Probing The Surface Reactivity Of Nanocrystals By The Catalytic Degradation Of Organic Dyes: The Effect Of Size, Surface Chemistry And Composition. *J. Mater. Chem. A* **2017**, *5*, 11917−11929.
(46) Däweritz, L.; Hey, R.; Berger, H. A Reflection High Energy Electron Diffraction Examination Of The Defect Structure In GaAs(001) Films Grown By Molecular Beam Epitaxy. *Thin Solid Films* **1984**, *116*, 165−174.
(47) Marks, L. D. Modified Wulff Constructions For Twinned Particles. *J. Cryst. Growth* **1983**, *61*, 556−566.
(48) Koivusalo, E. S.; Hakkarainen, T. V.; Galeti, H. V. A.; Gobato, Y. G.; Dubrovskii, V. G.; Guina, M. D. Deterministic Switching of the Growth Direction of Self-Catalyzed GaAs Nanowires. *Nano Lett.* **2019**, *19*, 82−89.
(49) Wang, N.; Cai, Y.; Zhang, R. Q. Growth of Nanowires. *Mater. Sci. Eng., R* **2008**, *60*, 1−51.
(50) De La Mata, M.; Leturcq, R.; Plissard, S. R.; Rolland, C.; Magén, C.; Arbiol, J.; Caroff, P. Twin-Induced InSb Nanosails: A Convenient High Mobility Quantum System. *Nano Lett.* **2016**, *16*, 825−833.
(51) Morales, A. M.; Lieber, C. M. A Laser Ablation Method for the Synthesis of Crystalline Semiconductor Nanowires. *Science (Washington, DC, U. S.)* **1998**, *279*, 208−211.
(52) Gamalski, A. D.; Voorhees, P. W.; Ducati, C.; Sharma, R.; Hofmann, S. Twin Plane Re-entrant Mechanism For Catalytic Nanowire Growth. *Nano Lett.* **2014**, *14*, 1288−1292.
(53) Wagner, R. S. On the Growth of Germanium Dendrites. *Acta Metall.* **1960**, *8*, 57−60.
(54) Ross, F. M.; Tersoff, J.; Reuter, M. C. Sawtooth Faceting In Silicon Nanowires. *Phys. Rev. Lett.* **2005**, *95*, 146104−4.
(55) Zamani, M.; Tütüncüoglu, G.; Martí-Sánchez, S.; Francaviglia, L.; Güniat, L.; Ghisalberti, L.; Potts, H.; Friedl, M.; Markov, E.; Kim, W.; Leran, J.-B.; Dubrovskii, V. G.; Arbiol, J.; Fontcuberta i Morral, A. Optimizing The Yield Of A-polar GaAs Nanowires To Achieve Defect-free Zinc Blende Structure And Enhanced Optical Functionality. *Nanoscale* **2018**, *10*, 17080−17091.
(56) Gorji Ghalamestani, S.; Heurlin, M.; Wernersson, L. E.; Lehmann, S.; Dick, K. A. Growth Of InAs/InP Core-shell Nanowires With Various Pure Crystal Structures. *Nanotechnology* **2012**, *23*, 285601−9.
(57) Gryaznov, V. G.; Heydenreich, J.; Kaprelov, A. M.; Nepijko, S. A.; Romanov, A. E.; Urban, J. Pentagonal Symmetry and Disclination In Small Particles. *Cryst. Res. Technol.* **1999**, *9*, 1091−1119.
(58) Faust, J.; John, H. The Growth Of Semiconductor Crystals From Solution Using The Twin Plane Reentrant-edge Mechanism. *J. Phys. Chem. Solids* **1964**, *25*, 1407−1415.
(59) Thomas, S. L.; King, A. H.; Srolovitz, D. J. When Twins Collide: Twin Junctions In Nanocrystalline Nickel. *Acta Mater.* **2016**, *113*, 301−310.
(60) Harmand, J. C.; Patriarche, G.; Glas, F.; Panciera, F.; Florea, I.; Maurice, J. L.; Travers, L.; Ollivier, Y. Atomic Step Flow on a Nanofacet. *Phys. Rev. Lett.* **2018**, *121*, 166101−5.
(61) Mayer, B.; Janker, L.; Loitsch, B.; Treu, J.; Kostenbader, T.; Lichtmannecker, S.; Reichert, T.; Morkötter, S.; Kaniber, M.; Abstreiter, G.; Gies, C.; Koblmüller, G.; Finley, J. J. Monolithically Integrated High-β Nanowire Lasers on Silicon. *Nano Lett.* **2016**, *16*, 152−156.
(62) Joyce, H. J. Growth and Characterisation of III−V Semiconductor Nanowires for Optoelectronic Device Applications. Thesis, 2009; pp 1−182.
(63) Kobayashi, T.; Matsumori, T.; Takayasu, I.; Makita, Y.; Nomura, T.; Kudo, K.; Izumi, T. Photoluminescence Spectra Of Undoped GaAs Grown By Molecular-beam Epitaxy At Very High And Low Substrate Temperatures. *J. Appl. Phys.* **2002**, *59*, 888−891.
(64) Koschel, W.; Briones, F.; Gladstone, J.; Patterson, G.; Stringfellow, G. B. Photoluminescence Of Carbon-implanted GaAs. *Appl. Phys. Lett.* **2003**, *39*, 581−582.
(65) Heiss, M.; Fontana, Y.; Gustafsson, A.; Wust, G.; Magen, C.; O'Regan, D. D.; Luo, J. W.; Ketterer, B.; Conesa-Boj, S.; Kuhlmann, A. V.; Houel, J.; Russo-Averchi, E.; Morante, J. R.; Cantoni, M.; Marzari, N.; Arbiol, J.; Zunger, A.; Warburton, R. J.; Fontcuberta i Morral, A. Self-assembled Quantum Dots In A Nanowire System For Quantum Photonics. *Nat. Mater.* **2013**, *12*, 439−444.
(66) Kim, W.; Fontcuberta i Morral, A.; Vukajlovic-Plestina, J.; Giunto, A.; Francaviglia, L.; Tütüncüoglu, G.; Potts, H.; Friedl, M.; Romero-Gomez, P.; Güniat, L. Anisotropic-Strain-Induced Band Gap Engineering in Nanowire-Based Quantum Dots. *Nano Lett.* **2018**, *18*, 2393−2401.
(67) Parkinson, P.; Joyce, H. J.; Gao, Q.; Tan, H. H.; Zhang, X.; Zou, J.; Jagadish, C.; Herz, L. M.; Johnston, M. B. Carrier Lifetime And Mobility Enhancement In Nearly Defect-free Core-shell Nanowires Measured Using Time-resolved Terahertz Spectroscopy. *Nano Lett.* **2009**, *9*, 3349−3353.
(68) Joyce, H. J.; Docherty, C. J.; Gao, Q.; Tan, H. H.; Jagadish, C.; Lloyd-Hughes, J.; Herz, L. M.; Johnston, M. B. Electronic Properties Of GaAs, InAs And InP Nanowires Studied By Terahertz Spectroscopy. *Nanotechnology* **2013**, *24*, 214006−7.
(69) Stettner, T.; Zimmermann, P.; Loitsch, B.; Döblinger, M.; Regler, A.; Mayer, B.; Winnerl, J.; Matich, S.; Riedl, H.; Kaniber, M.; Abstreiter, G.; Koblmüller, G.; Finley, J. J. Coaxial GaAs-AlGaAs Core-multishell Nanowire Lasers With Epitaxial Gain Control. *Appl. Phys. Lett.* **2016**, *108*, 011108−5.
(70) Guniat, L.; Caroff, P.; Fontcuberta i Morral, A. Vapor Phase Growth of Semiconductor Nanowires: Key Developments and Open Questions. *Chem. Rev.* **2019**, DOI: 10.1021/acs.chemrev.8b00649.
(71) de la Mata, M.; Zamani, R. R.; Martí-Sànchez, S.; Eickhoff, M.; Xiong, Q.; Fontcuberta i Morral, A.; Caroff, P.; Arbiol, J. The Role of Polarity in Non-Planar Semiconductor Nanostructures. *Nano Lett.* **2019**, DOI: 10.1021/acs.nanolett.9b00459. Accepted.

DOI: 10.1021/acsnano.9b01546
ACS Nano XXXX, XXX, XXX−XXX